CHALMERS
UNIVERSITY OF TECHNOLOGY

Analytical models for initial and intermediate stages of sintering of additively manufactured stainless steel

Acta Materialia 249 (2023) 118822

Contents lists available at ScienceDirect

Acta Materialia

journal homepage: www.elsevier.com/locate/actamat

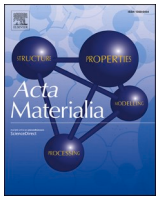

Full length article

Analytical models for initial and intermediate stages of sintering of additively manufactured stainless steel

Alberto Cabo Rios [a,b,*], Eugene Olevsky [b,c], Eduard Hryha [a], Mats Persson [d], Rajendra K. Bordia [e]

[a] Department of Industrial and Materials Science, Chalmers University of Technology, Gothenburg, Sweden
[b] Mechanical Engineering, San Diego State University, San Diego, USA
[c] NanoEngineering, University of California, La Jolla, San Diego, USA
[d] Digital Metal AB, Höganäs, Sweden
[e] Department of Materials Science and Engineering, Clemson University, Clemson, SC 29634 United States

ARTICLE INFO

Keywords:
Binder jetting
Additive manufacturing
Sintering
Shrinkage
Stainless steel

ABSTRACT

In isotropic pressure-less sintering continuum mechanics models, densification kinetics is driven by the balance between the effective sintering stress and bulk viscosity. In components manufactured by binder jetting (BJ), the green structure created by the arrangement of spherical powder particles during printing is characterized by its high porosity (40–50%). This leads to a wide porosity range for the initial and intermediate sintering stages, where a complex combination of diffusion mechanisms drives matter redistribution through the porous compact. In this paper, a comprehensive analysis of the porosity effect on the resistance to densification of 316L BJ during sintering was performed by avoiding other highly influencing factors like δ-ferrite phase transformation. Different normalized bulk moduli expressions, inspired by Skorohod, Hsueh, and Abouaf sintering models, are used in the framework of the continuum theory of sintering. A new material constants determination algorithm based on the sintering experiments design and non-linear analysis of the model was proposed. This evidenced the critical importance of the experimental data collection for the determination of the required sintering model constants. Accordingly, material shear viscosity and normalized bulk viscosity constants were successfully determined based on dilatometry and grain size experimental data. The bulk moduli proposed comprise physical parameters which depend on the interparticle stress distribution or the initial high reactivity of the BJ compacts. The variation of powder size distribution and/or arrangement would potentially impact the determination of these constants in the normalized bulk moduli.

1. Introduction

Solid-sate sintering of metal powders is a thermally activated diffusional process, where the matter transport occurs along different diffusion paths (e.g. grain boundary, bulk or surface diffusion). At the atomic scale, sintering is driven by the diffusion fluxes dictated by the microstructure evolution, temperature and pressure applied. At the continuum scale, free-sintering can be described as the viscoelastic deformation of a porous body, where volume deformation is caused by material flow to and around pores [1]. Therefore, there is a direct relationship between the complex atomic-scale diffusional problem and the macroscale viscous flow in the porous body. Previous studies [2] demonstrated the relationship between the complex combination of different diffusion mechanisms and the shear viscosity parameter η that appears in the stress-strain relationships for porous bodies under sintering. Thus, despite the diffusional nature of sintering in powder metallurgy, the assumption of a porous viscoelastic body to model the sintering is suitable.

Powder bed binder jetting (BJ) is a multi-step additive manufacturing (AM) process, defined as a "process in which a liquid bonding agent is selectively deposited to join powder particles" [3]. Amongst the operations consisting the BJ process of metallic materials, sintering is typically the critical step where the brown (debinded) component evolves until the final geometry and properties are reached. During sintering, BJ components typically undergo severe shrinkages (up to 50%) caused by low green densities of the as-printed components that is typically between the apparent and tap density of the powder used [4,5]. Also, the different printing mechanisms (e.g. recoating, roller movement and binder deposition) may introduce non-homogeneities in

* Corresponding author: Department of Industrial and Materials Science, Chalmers University of Technology, Hörsalsvägen 7, Gothenburg 412 58, Sweden.
E-mail address: cabo@chalmers.se (A. Cabo Rios).

https://doi.org/10.1016/j.actamat.2023.118822
Received 3 October 2022; Received in revised form 11 February 2023; Accepted 27 February 2023
Available online 2 March 2023

Nomenclature

$\dot{\boldsymbol{\varepsilon}}_s$	sintering strain rate term (s^{-1})
K	effective bulk viscosity $(Pa{\cdot}s)$
$\boldsymbol{I}$	identity tensor
ρ	density
ρ_f	final density
θ	porosity
$\dot{\theta}$	porosity elimination rate (s^{-1})
$\boldsymbol{\sigma}_{ij}$	stress tensor $(N{\cdot}m^2)$
$\dot{\boldsymbol{\varepsilon}}_{ij}$	strain rate tensor (s^{-1})
$\dot{e}$	trace of the strain rate tensor (s^{-1})
δ_{ij}	kronecker delta function
$\dot{\varepsilon}_x$	x component of strain rate tensor (s^{-1})
φ	normalized shear modulus
ψ	normalized bulk modulus
P_L	sintering stress (Pa)
α	surface energy $(J{\cdot}m^{-2})$
r	particle mean radius (m)
η_0	material shear viscosity $(Pa{\cdot}s)$
A_0	viscosity pre-exponential factor $(Pa{\cdot}s)$
Q	viscosity activation energy $(J{\cdot}mol^{-1})$
R	gas constant 8.314 $(J{\cdot}mol^{-1}{\cdot}K^{-1})$
T	temperature (K)
t	time (t)
$\dot{G}$	grain growth rate $(m{\cdot}s^{-1})$
G	grain size diameter (m)
r_0	initial grain size radius (m)
k_0	grain growth pre-exponential factor $(\mu m^3{\cdot}s^{-1})$
Q_G	grain growth activation energy $(J{\cdot}mol^{-1})$
ρ_c	grain growth critical density
k_G	grain size scaling factor
A	fitting parameter
B	fitting parameter
θ_c	critical porosity fitting parameter

the powder bed packing [6]. 316L stainless steel is one of the material systems most frequently used in BJ, which has some sintering-related particularities. Previous research exposed the key influence of the δ-ferrite phase transformation on the sintering densification of 316L components [4]. Also, varied extent of sintering shrinkage anisotropy was revealed [5]. When present, these phenomena must be included in the modelling approach. However, if sintering is performed below the phase transformation temperature and anisotropy is insignificant, traditional isotropic pressure-less (free) solid-state sintering models can be used to predict the macro-structure of BJ components during sintering.

Despite the discrete nature of the powder particles, the macroscale modelling of powder compacts as a continuum media has been significantly developed during the last decades [1,7]. Particularly, simulations of sintering by the Finite Element Method (FEM) have been demonstrated to be suitable for the prediction of densification and geometrical evolution [1,8–17]. In general, the free sintering constitutive law term corresponding to isotropic sintering densification can be expressed as $\dot{\varepsilon}_s = \frac{-P_L}{3K}\boldsymbol{I}$ [1]. The main difference between different models is in terms of the differences in the effective sintering stress P_L and the effective bulk viscosity K. The effective bulk viscosity depends on the temperature and porosity $K = \eta_0(T){\cdot}\psi(\theta)$, where η_0 is the shear viscosity of the fully dense material and ψ is the normalized bulk viscosity. At the continuum scale, ψ physically represents the influence of the porous structure morphology on the resistance of the powder compact to densification (i.e. volumetric shrinkage). Several porosity-dependent expressions which characterize the normalized bulk viscosity have been proposed. Some authors use different analytical expressions for the different stages of sintering [18,19]. Also, the use of expressions with process-related parameters (e.g. green porosity) have been suggested [18,20,21]. Others are only dependent on the global porosity value of the powder compact [22,23]. These analytical expressions can be derived from different mechanical models. In this study, the models developed by Olevsky [1], Abouaf [24] or Hsueh [20] are of special interest.

The continuum theory of sintering [1] developed by Olevsky is based on the 3D stochastic analysis performed by Skorohod [23]. The porous compact was considered as a two-phase material, where the powder corresponds to the incompressible viscous matrix and the pores are the secondary dispersed phase. Normalized bulk and shear moduli were derived assuming small ($\theta \ll 1$) and randomly dispersed spherical pores. Then, an analysis for larger porosities was done by considering larger cylindrical pores, representative of the interconnected porosity. The combined theoretical analysis for the range of porosities between 0 and 2/3 led to the normalized bulk viscosity expression $\psi = 2(1-\theta)^3/3\theta$ which only depends on the global porosity value. Thus, this expression is used for the broad sintering porosity range [0, 2/3] and contains no material specific parameters.

Hsueh's phenomenological model [20], based on the diffusional creep of porous solids, use the following effective shear viscosity expression $\eta = \eta_0(\rho/\rho_f)^p(1-\rho/\rho_f)^{-\lambda}$. The physical definition of the parameters are related to the stress concentrations generated at the inter-particle contacts within the powder compact. The power law function led to excellent correlation with sintering density experimental data for Al_2O_3, using p and λ as fitting parameters. Here, the reference shear viscosity η_0 represents the material and temperature dependent term of the effective shear viscosity evolution. In a recent study, Olevsky et al. [25] applied kinetic Monte-Carlo (KMC) mesoscale simulation results to estimate the normalized bulk viscosity at the continuum scale. The proposed normalized bulk viscosity term $2(1-\theta)^c/3\theta^d$ was analogous to the expression from Hsueh's model. Discrepancies were revealed when compared to the Skorohod expression, which were attributed to the dimensionality difference: 2D mesoscale simulations vs. 3D stochastic analysis of Skorohod. Yet, this study suggests that modelling a specific mesoscale structure at the continuum level required the adjustment of the normalized bulk viscosity.

An elasto-viscoplastic constitutive equation was developed by Abouaf to model the sintering phenomena during hot isostatic pressing (HIP) [24]. Here, the porosity-dependent plastic yield function was directly obtained from experimental measurements. Later, Besson and Abouaf described the so-called "snap-through" buckling process at low densities during sintering of a porous compact [26]. They defined a density dependent function which includes the density limit under which particles rearrangement caused by this process occurs. This idea was recently used in [27] to modify the Skorohod normalized bulk viscosity to account for the effect of rearrangement occurring for powder compacts with low green densities. Here, an equivalent critical porosity θ_c was included within the Skorohod expression $\psi = 2(\theta_c-\theta)^3/3\theta$, which forces ψ to zero at porosity equal to θ_c. The value θ_c is tailored to experimental data and is typically close to the porosity in the green state. Similarly, this critical porosity concept has been used to fit the normalized shear and bulk moduli to experimental data [28].

Consolidation of binder jetted parts is performed mostly by conventional free sintering. However, a particular green porous structure is attained by the specifics of the particle arrangement during printing. This phenomenon makes it necessary to evaluate and find an appropriate model for the sintering of binder-jet-manufactured components.

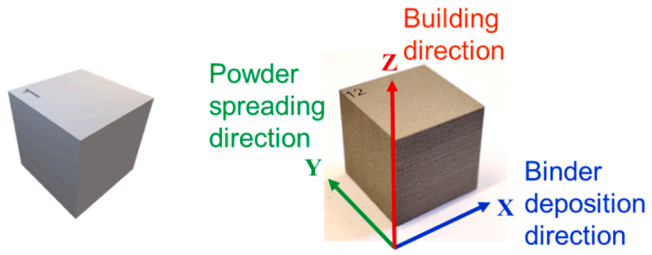

Fig. 1. Images of the BJ cubical samples: pre-sintered sample (right) and CAD geometry (left).

Recent studies dealing with sintering modelling of 316L components are focused on high temperature sintering to reach close to full density [16, 29–32]. However, little attention has been placed on the initial and the intermediate sintering stages of the BJ components, when the porous structure morphology has a higher impact on the sintering behavior. Therefore, a model that precisely describes the sintering of BJ parts caused by its characteristic green porous structure is of contemporary interest.

The objective of this study is to develop and evaluate sintering models considering the influence of different normalized bulk viscosity expressions for BJ samples. Two parameterized normalized bulk viscosity expressions, inspired by Hsueh and Abouaf models, are proposed in this study. Also, Skorohod theoretical normalized bulk viscosity formulation is assessed. One of the challenges of using parameterized non-linear expressions of the normalized bulk viscosity is to find a suitable method to determine the model parameters by using the appropriate experimental data. A non-linear data-fitting method was successfully used in this study to find the different material constitutive parameters. Several sintering experiments were performed at temperatures below the δ-ferrite phase transformation for a wide range of dwell times (2 min to 10 h). Also, the grain size was measured for each sintered sample and a porosity-dependent grain growth kinetic equation was implemented to include its influence during sintering. The method proposed can be generalized for the determination of the sintering model parameters of other BJ 316L stainless-steel samples manufactured using different powder size distribution and/or printing parameters.

2. Experiments and methods

Cubic samples with dimensions 10 × 10 × 10 mm^3 were printed using the DM P2500 Binder Jetting system (Digital Metal AB) with a layer thickness of 42 μm. Samples were debinded in air at 345 °C for 2 h. Then, samples were consolidated by pre-sintering in an industrial batch furnace under pure hydrogen atmosphere following 5 °C/min heating rate up to 900 °C with a dwell time of 1 hour and final furnace cooling down to room temperature.

The pre-sintered samples were subjected to dilatometry sintering experiments using Netzsch DIL 402C, where the pushrod was aligned with the sample Z axis (see Fig. 1). Interrupted sintering trials were performed at 1000, 1100, 1200 and 1300 °C with a dwell time of 2, 60, 150 and 600 min with a heating rate of 5 °C/min and cooling rate of 30 °C/min in hydrogen atmosphere (purity 6.0). The external dimensions and mass of the cubic samples were measured systematically before and after sintering to calculate the relative density as follows:

$$\rho = (1-\theta) = \frac{m}{(L_x \cdot L_y \cdot L_z)\cdot \rho_{full}} \quad (1)$$

where m is the sample mass in grams, L are the dimensions along the different directions and $\rho_{full} = 7.95\ mg/mm^3$ is the theoretical density for the 316L alloy. Also, the relative density of the sintered samples was measured via the Archimedes principle [33].

Sintered samples were cut along the three orthogonal planes (XZ, YZ, XY), mounted and metallography prepared. The grain structure was revealed by aqueous 40% HNO_3 electrochemical etching. Then, 25 images evenly distributed across each sample's cross-section were acquired by using the automated Zeiss Axioscope 7 light optical microscope (LOM) system. Finally, LOM images were postprocessed combining Fiji and MATLAB image analysis to measure the grain size following the line-sampled linear intercept length method [34]. In parallel, electron backscattered diffraction (EBSD) was done using the LEO Gemini 1550 SEM equipped with a Nordlys II detector (Oxford Instruments) and the

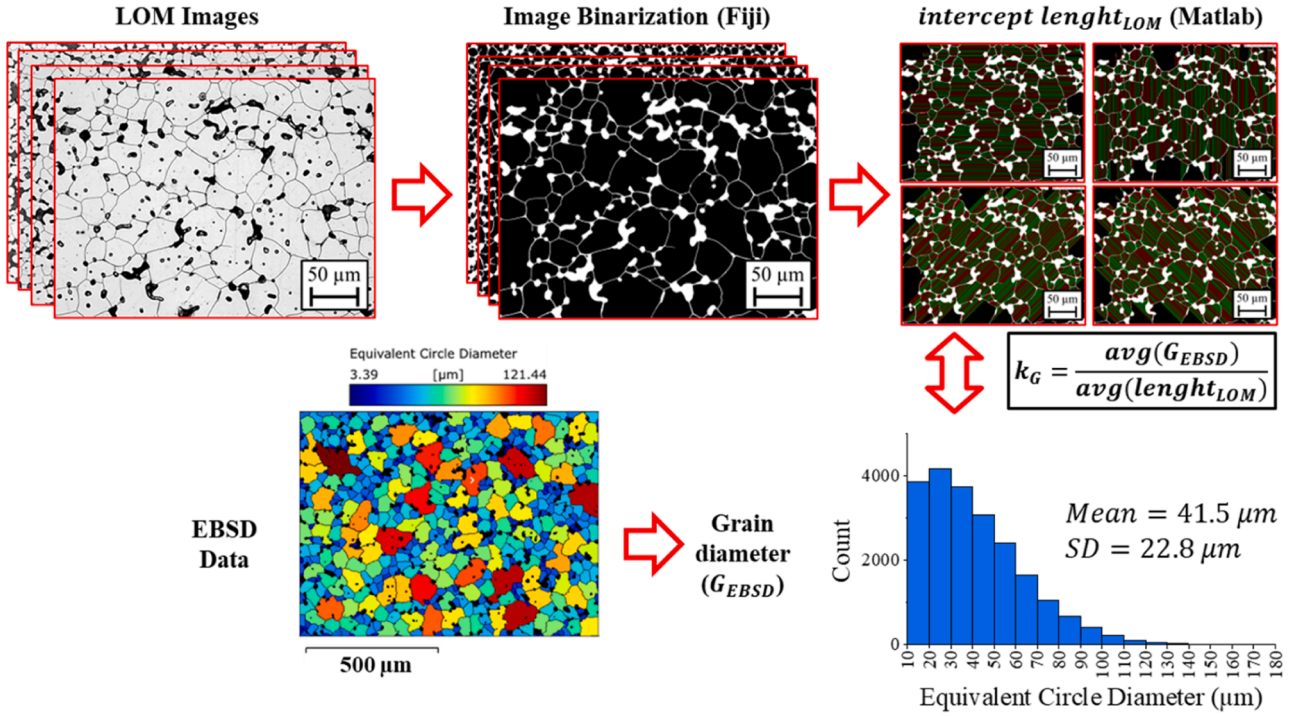

Fig. 2. Ilustration of the method used to obtain the average grain size value for each sintered sample by image analysis of LOM micrographs and EBSD data.

HKL Channel 5 processing software to obtain the crystallographic information of the microstructure. The average equivalent circle diameter characterized by EBSD was used to calibrate the average linear intercept length measurements [35]. Then, a factor $k_G$was calculated and applied to all the average linear intercept lengths to obtain the equivalent circle diameter (see Fig. 2).

3. Theory: constitutive equation and modelling

3.1. Constitutive equation for free sintering

The continuum theory of sintering [1] is used as a basis for the model development in this study. Specifically, the linear-viscous case can be used to model the pressure-less sintering behavior of the micron-sized BJ powder . Therefore, the behavior of the respective continuum medium can be described by the following constitutive equation, which defines the relation between the stress and the strain rate tensors:

$$\boldsymbol{\sigma_{ij}} = 2\eta_0\left[\varphi\dot{\boldsymbol{\varepsilon}}_{\boldsymbol{ij}} + \left(\psi - \frac{1}{3}\varphi\right)\dot{e}\delta_{ij}\right] + P_L\delta_{ij} \tag{2}$$

where η_0 is the shear viscosity of the porous body's skeleton material (i.e. shear viscosity of the fully dense body), P_L is the effective sintering stress and δ_{ij} is the Kronecker delta function. φ and ψ are functions of porosity that characterize the normalized shear and bulk moduli of the porous compact. $\dot{e}$ is the first invariant of the strain rate tensor, which corresponds to the volumetric shrinkage rate.

Particularly, the pressure-less isotropic case constitutive equation can be derived by considering negligible external stresses and isotropic shrinkage rate as follows:

$$\boldsymbol{\sigma_{ij}} = \begin{pmatrix} 0 & 0 & 0 \\ 0 & 0 & 0 \\ 0 & 0 & 0 \end{pmatrix} \tag{3}$$

$$\dot{\boldsymbol{\varepsilon}}_{\boldsymbol{ij}} = \begin{pmatrix} \dot{\varepsilon}_x & 0 & 0 \\ 0 & \dot{\varepsilon}_y & 0 \\ 0 & 0 & \dot{\varepsilon}_z \end{pmatrix} \text{ assuming isotropy : } \dot{\boldsymbol{\varepsilon}}_{\boldsymbol{ij}} = \begin{pmatrix} \dot{\varepsilon}_z & 0 & 0 \\ 0 & \dot{\varepsilon}_z & 0 \\ 0 & 0 & \dot{\varepsilon}_z \end{pmatrix} \tag{4}$$

Then, introducing Eqn. (3) and (4) in Eqn. (2) leads to the following analytical form of the pressure-less isotropic constitutive relationship:

$$0 = 2\eta_0\left[\varphi\dot{\varepsilon}_z + \left(\psi - \frac{1}{3}\varphi\right)3\dot{\varepsilon}_z\right] + P_L \tag{5}$$

The reduced expression can be obtained:

$$3\dot{\varepsilon}_z = -\frac{P_L}{2\eta_0\psi} \tag{6}$$

The mass conservation equation can be used to determine the porosity evolution as a function of the volumetric shrinkage rate as follows:

$$\frac{\dot{\theta}}{(1-\theta)} = \dot{\varepsilon}_x + \dot{\varepsilon}_y + \dot{\varepsilon}_z = 3\dot{\varepsilon}_z \tag{7}$$

Finally, the equation that describes the porosity evolution during sintering is derived by including the mass conservation Eqn. (7) into the sintering Eqn. (5):

$$\frac{d\theta}{dt} = -\frac{(1-\theta)P_L}{2\eta_0\psi} \tag{8}$$

3.2. Experimental determination of sintering model parameters by non-linear regression method: Skorohod, Abouaf and Hsueh normalized bulk viscosities

Eqn. (8) describes the rate of porosity evolution as a function of the porosity θ, effective sintering stress P_L, normalized bulk viscosity ψ and skeleton material shear viscosity η_0. At the same time, P_L and ψ are functions of the porous structure morphology and topology. Besides, the characteristic temperature-dependent behavior of the powder material shear viscosity η_0 is represented by an Arrhenius-type function [36] as follows:

$$\eta_0 = A_0 T exp\left(\frac{Q}{RT}\right) \tag{9}$$

where A_0 and Q are material constants that should be determined for each powder alloy.

The following expression for the effective sintering stress is used in the model [1]:

$$P_L = 3\alpha\frac{(1-\theta)^2}{r_0} \tag{10}$$

where α is the specific surface energy [J /m^2] and r_0 is the powder particle radius. Here, r_0 is assumed to be equivalent to the grain radius, which evolves during sintering [37,38]. This assumption is taken to include the effect of the grain growth, which decreases the sintering stress during the sintering process.

In this work, different normalized bulk viscosity expressions ψ are evaluated for the modelling of the BJ porous samples. Initially, the theoretical analytical expression derived by Skorohod [23], is considered as a reference:

$$\psi = \frac{2}{3}\frac{(1-\theta)^3}{\theta} \tag{11}$$

Then, two different cases of parametrized ψ expressions are studied. These two expressions ψ_1 and ψ_2 are inspired by Hsueh [20] and Abouaf [24] model, respectively:

$$\psi_1(A,B,\theta) = \frac{2}{3}\frac{(1-\theta)^A}{\theta^B} \tag{12}$$

$$\psi_2(\theta_c,\theta) = \frac{2}{3}\frac{(\theta_c-\theta)^3}{\theta} \tag{13}$$

Originally, Hsueh utilized a power law function for porosity-dependent term of the effective bulk viscosity, because of its precise correlation with the experimental data [20]. This expression contains two fitting parameters (A, B), related to the interparticle stress concentration of the powder compact analyzed. The expression inspired in Abouaf's model includes a critical porosity parameter (θ_c) such that the effective bulk viscosity approaches zero when the porosity approaches the green porosity [26–28].

Introducing Eqn. (9), (10), and the different normalized bulk viscosity expressions ψ (11), ψ_1 (12) and ψ_2 (13) into the sintering Eqn. (8), we can obtain the following generalized differential equation for the evolution of porosity during sintering:

$$\frac{d\theta}{dt} = -\frac{9}{\frac{A_0}{\alpha}Texp\left(\frac{Q}{RT}\right)2G}f(\theta) \tag{14}$$

where the function $f(\theta)$ de-convolutes the porosity variable θ, and depends on the bulk modulus expression used. Therefore, a specific $f(\theta)$ is derived for each case:

$$f(\theta)_{\psi_{Skorohod}} = \theta \tag{15}$$

$$f(\theta)_{\psi_1} = \frac{\theta^B(1-\theta)^3}{(1-\theta)^A} \tag{16}$$

$$f(\theta)_{\psi_2} = \frac{\theta(1-\theta)^3}{(\theta_c-\theta)^3} \tag{17}$$

The time dependent porosity and temperature data $(\theta, \dot{\theta}, T)$ can be

Table 1
Density and shrinkage results from measurements before and after dilatometry sintering experiments.

SAMPLE	Pre-sintered density	ΔX (%)	ΔY (%)	ΔZ (%)	Sintered Density	Sintered Density (Archimedes)
1000 °C - 2min	57.2%	1.3%	1.4%	1.6%	58.4%	59.3%
1100 °C - 2min	57.3%	3.1%	3.4%	3.3%	61.7%	62.5%
1200 °C – 2min	57.3%	5.4%	5.4%	5.5%	66.3%	67.3%
1300 °C–2min	57.4%	7.8%	7.9%	8.3%	72.1%	72.9%
1000 °C–60min	57.2%	2.9%	3.1%	3.2%	61.6%	62.6%
1100 °C–60min	57.1%	5.7%	5.7%	6.0%	67.0%	67.6%
1200 °C–60min	57.3%	8.3%	8.2%	8.6%	72.8%	73.6%
1300 °C–60min	57.1%	10.3%	10.4%	11.0%	78.2%	79.3%
1000 °C–150min	57.1%	4.3%	4.3%	4.6%	64.1%	65.2%
1100 °C–150min	57.2%	7.3%	7.4%	7.7%	70.7%	71.4%
1200 °C–150min	57.4%	9.7%	9.8%	10.3%	76.7%	77.7%
1300 °C–150min	57.1%	11.4%	11.5%	12.5%	81.6%	83.2%
1000 °C–600min	57.2%	7.1%	7.0%	7.5%	70.1%	71.0%
1100 °C–600min	57.0%	10.1%	10.1%	10.9%	77.5%	78.6%
1200 °C–600min	57.2%	11.9%	12.0%	12.8%	82.6%	84.1%
1300 °C–600min	57.1%	13.4%	13.4%	14.4%	87.1%	88.7%

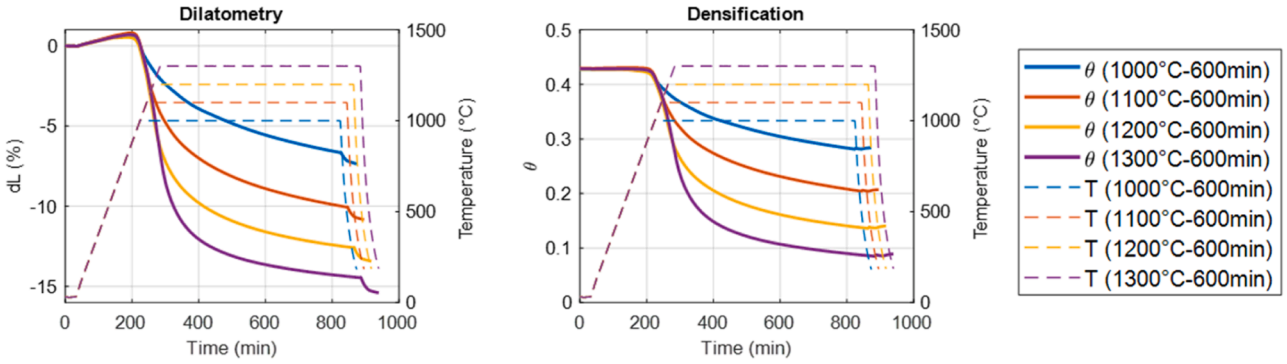

Fig. 3. Dimensional changes (left) and density evolution calculated from dilatometry sintering experiment data of the samples sintered for 600 min.

obtained from the dilatometry experiments, and the grain size (G) is calculated by the kinetic equation described in Section 3.3 below. Therefore, the unknown material constants related to the particle material shear viscosity ($\frac{A_0}{\alpha}$, Q) in Eqn. (14) need to be identified. Also, the normalized bulk viscosity parameters A, B and θ_c need to be determined for each expression ψ_1 and ψ_2, respectively. The non-linear nature of the parametrized bulk moduli expressions proposed (ψ_1 and ψ_2,) requires the use of non-linear regression methods [39]. Also, the stability of the numerical method used for the constant's determination must be analyzed and discussed, considering the experimental datasets used during the process.

3.3. Porosity adjusted grain growth model during sintering

The kinetic equation used by Olevsky et al. [8] is used to predict the grain growth evolution during sintering. The grain size is calculated by solving the following kinetic equation, where the grain growth is driven by the density ρ and temperature T during sintering:

$$\frac{dG}{dt} = \frac{k_0}{3G^2}\left(\frac{1-\rho_c}{2-\rho_c-\rho}\right)^{3/2}\exp\left(\frac{-Q_G}{RT}\right) \tag{18}$$

In this non-linear differential equation, the grain growth pre-exponential term k_0 and activation energy Q_G define the temperature-dependent behavior of the grain growth. Also, a critical density parameter ρ_c accounts for the grain boundary pore pinning effect on the grain growth. This density function tends to 1 as the sample tends to full density, therefore the kinetic equation converges to the traditional grain growth equation for a fully dense body [40].

4. Results and discussion

4.1. Porosity evolution during dilatometry experiments

An essential step in this study is the post-processing of the experimental raw data to obtain the sintering model parameters. Table 1 shows the pre-sintered and sintered relative density before and after the dilatometry experiments, along with the sintering shrinkages measured along the three main directions of the cubical samples. The pre-sintered density difference between samples is small, with an average value of 57.2 ± 0.1%. This evidence the typically low initial green density of BJ samples, lower than the powder tap density (62.9%). Note that Archimedes sintered density values were slightly larger (~1%) than the geometry-based density values [4].

As shown in Table 1, the dimensional shrinkage along the three orthogonal directions is almost the same for all thermal treatments (maximum difference of ~1%). Therefore, isotropic sintering behavior of the BJ samples studied can be assumed, especially when compared with previous results from BJ sintering literature where measured shrinkages largest difference between the different directions can be up to ~ 4.5% [4–6]. Then, porosity evolution during sintering was derived using the mass conservation Eqn. (7) and shrinkage data obtained from dilatometry. Finally, the required experimental sintering data for the parameter's identification is available $\theta, \dot{\theta}, T = f(t)$. Fig. 3 shows the shrinkage and porosity curves derived from the dilatometry sintering tests performed with a dwell time of 600 min.

4.2. Determination of grain growth parameters

The sintering behavior of powder metallurgy components is affected by the grain size evolution, specially within the low porosity range,

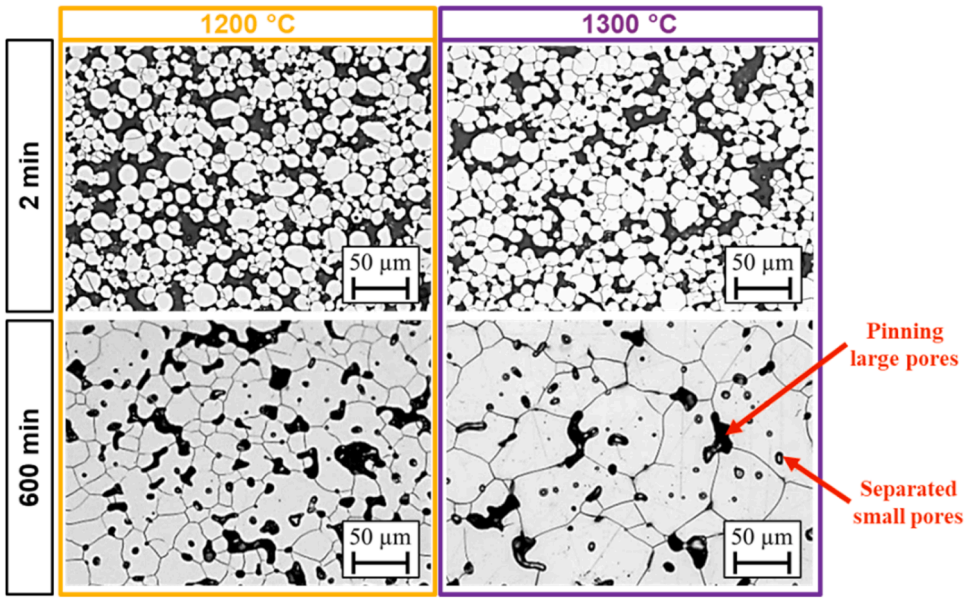

Fig. 4. Illustration of LOM images used for the sintered sample's grain size measurements showing the pinning effect of large pores.

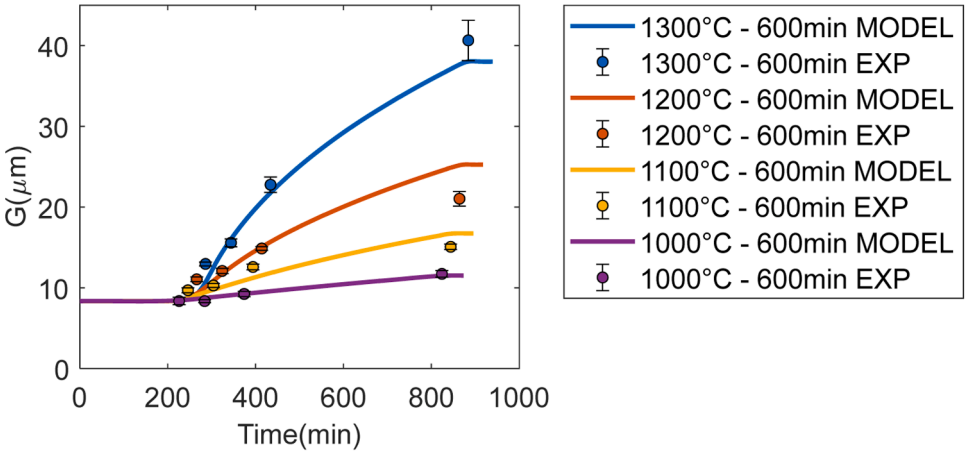

Fig. 5. Grain growth evolution during sintering of 316L BJ samples.

Table 2
Grain growth kinetics parameters identified for the 316L BJ samples.

$k_0[\mu m^3/s]$	$Q_G[KJ/mol]$	ρ_c
29.65 e-5	164.8	0.948

because of the rapid grain growth during the final stage of sintering [28, 37,38,41,42]. However, other variables, such as sintering time or pore size and distribution, can induce substantial grain growth even within a range of higher porosity levels >10%, where grain growth is typically very limited by the presence of porosity. For the shorter times, negligible grain growth was observed during sintering. But sintering at higher temperatures and longer dwell times, for instance at 1300 °C and 600 min (see Fig. 4), indicated substantial grain growth. Qualitatively it can be observed that during sintering a mixture of large and small pores develops (from the original interconnected green porosity) with increasing time and/or temperature. It was observed that the small pores were separated from the grain boundaries during sintering. But the largest pores still pin the grain boundaries at higher temperatures and long dwell times, still reducing the grain growth kinetics. Therefore, despite the relatively large porosity, substantial grain growth during the intermediate stage of sintering was observed.

The LOM images collected were used to obtain the average grain diameter by the linear intercept method for each sintered sample. Besides, the EBSD analysis of the sample sintered at 1300 °C for 600 min was used to derive the scaling factor k_G, used to calibrate the measurements from LOM image analysis (see Fig. 2). An EBSD scan area of 4 mm x 4 mm was considered, where a total count of 21,407 grains were detected with a mean equivalent circle diameter of 41.5 µm. Then, dividing by the averaged value calculated by the intercept method of 29.3 µm led to a factor of $k_G = 1.417$. The standard method [35] suggests the use of a general factor of 1.5, which is close to the specific value obtained for this case.

The experimental grain size data, together with the porosity data calculated from dilatometry, are used to fit the parameters of the grain growth kinetic equation described in Section 3.3. The lowest grain size measured was used as an initial condition for solving Eqn. (18). Fig. 5 shows the experimental grain diameter together with the model results using parameters in Table 2. The critical density ($\rho_c \sim 94.8\%$) correlates with the value used in the previous study [8] and the activation energy value agrees with the values reported in [43].

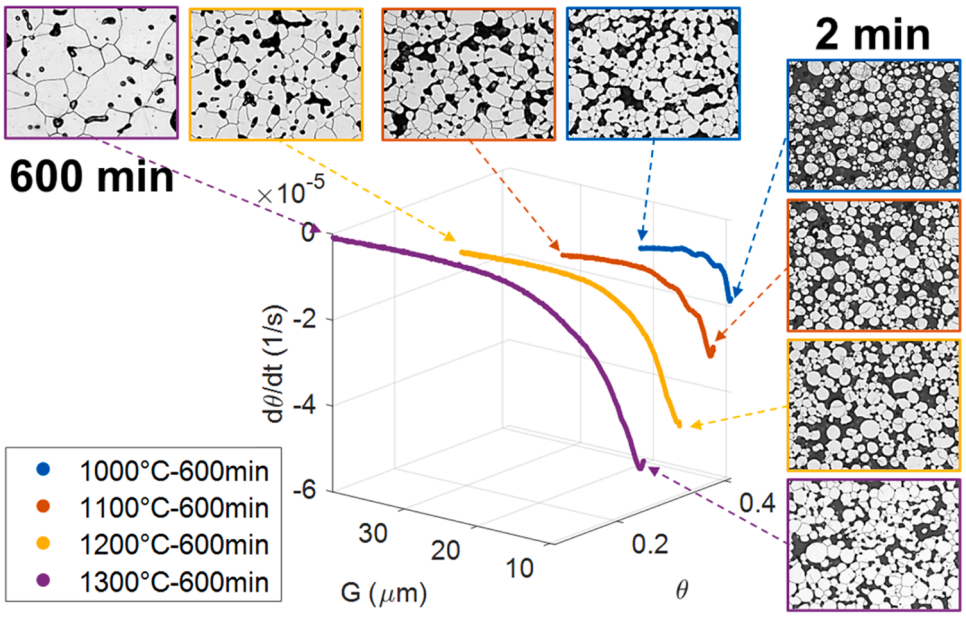

Fig. 6. Sintering experimental data $(\theta, \dot{\theta}, T, G)$ used for the model parameters identification.

Table 3
Normalized bulk viscosity ψ, porosity-dependent function $f(\theta)$ and fitted parameters corresponding to the different models used in this study.

	ψ	$f(\theta)$	A_0/α $[s\ m^{-1}K^{-1}]$	Q $[K\ J\ mol^{-1}]$	A	B	θ_C
$\psi_{skorohod}$	$\frac{2}{3}\frac{(1-\theta)^3}{\theta}$	θ	35.53	144.1	–	–	–
ψ_1	$\frac{2}{3}\frac{(1-\theta)^A}{\theta^B}$	$\frac{\theta^B(1-\theta)^3}{(1-\theta)^A}$	2.03	217.2	11.35	0.49	–
ψ_2	$\frac{2}{3}\frac{(\theta_c-\theta)^3}{\theta}$	$\frac{\theta(1-\theta)^3}{(\theta_c-\theta)^3}$	1.82	220.1	–	–	0.508

4.3. Determination of normalized bulk viscosity parameters via non-linear regression method: analysis of different expressions

Several sintering curves have been collected from dilatometry experiments at 4 different temperatures and 4 different dwell times. The datasets from the longest dwell times of 600 min contain the highest amount of data points within a wider porosity range. Besides, the dataset selection should be driven by the form of the non-linear Eqn. (20) derived. The use of data from a single experiment was analyzed and compared with the use of the complete experimental dataset in Appendix A. This proves the relevance of an appropriate collection of experiments in the development of sintering models when complex non-linear equations are derived. Moreover, a numerical stability test of the parameter's determination was performed and is crucial for the modelling methodology developed in this study. Consequently, the isothermal data points at 1000 °C, 1100 °C, 1200 °C and 1300 °C, are used for the determination of the sintering model parameters.

This 'cloud' of experimental data points $(\theta, \dot{\theta}, T)$ and G (calculated from the model) in Fig. 6 is used to identify the different expressions constants of the analytical sintering model, which describes the porosity evolution for each case of the normalized bulk viscosity term analyzed in this work:

$$\frac{d\theta}{dt} = -\frac{9}{\frac{A_0}{\alpha}\mathrm{Texp}\left(\frac{Q}{RT}\right)2G}\cdot f(\theta) \tag{19}$$

The material shear viscosity $(A_0/\alpha,\ Q)$ and the parameters for the normalized bulk viscosity, for each case are presented in Table 3. The material shear viscosity curves for the ψ_1 and ψ_2 cases are similar (see Fig. 7). In contrast, the absence of any fitting parameter in $\psi_{Skorohod}$ make the material shear viscosity constants in η_0 the only fitting constants. This causes a significant difference on A_0/α and Q values, compared with the other cases, and leads to a shear viscosity more than one order on magnitude lower (see Fig. 7(a)). The material shear viscosity η_0 would have a direct impact on the potential shear deformation of complex geometries caused by external forces (e.g. gravity). At the continuum scale, the shear distortion is driven by the effective shear viscosity $G = \eta_0 \cdot \varphi$, where φ is the porosity dependent expression of the effective shear viscosity [1]. Lower η_0 values would typically lead to larger shape distortions under external forces. Further research is ongoing to study the distortion of BJ specimens under external forces.

Mathematically, ψ_1 and ψ_2 can be defined as two variations of the Skorohod theoretical expression. ψ_1 is inspired by Hsueh modelling studies [20], where the fitting parameters A and B (which depends on the interparticle stress distribution) determines the resistance to densification within the low and high porosity values range, respectively. In this case, the fitting produces a large variation of the function at high porosity values where the exponent $A = 11.548$ differs from the corresponding Skorohod exponent of 3. On the other hand, ψ_2 was previously used in [27] and inspired by Abouaf's model [24,26]. Here, the critical porosity constant θ_C [27] was introduced to account for the high reactivity of the initial porous compact. For BJ samples, the same effect can be expected owing to the high interconnected green porosity due to the absence of compaction prior to sintering. At the critical porosity $\theta_C = 0.508$, the bulk modulus tends towards zero (see Fig. 7(b)). As expected, a value relatively close to the green porosity ($\theta_0 = 0.428$) was obtained. ψ_1 and ψ_2 showed a shift to lower values with respect to the theoretical Skorohod expression. The largest difference between ψ_2, ψ_2 *and* $\psi_{Skorohod}$ was found within the high porosity region while it

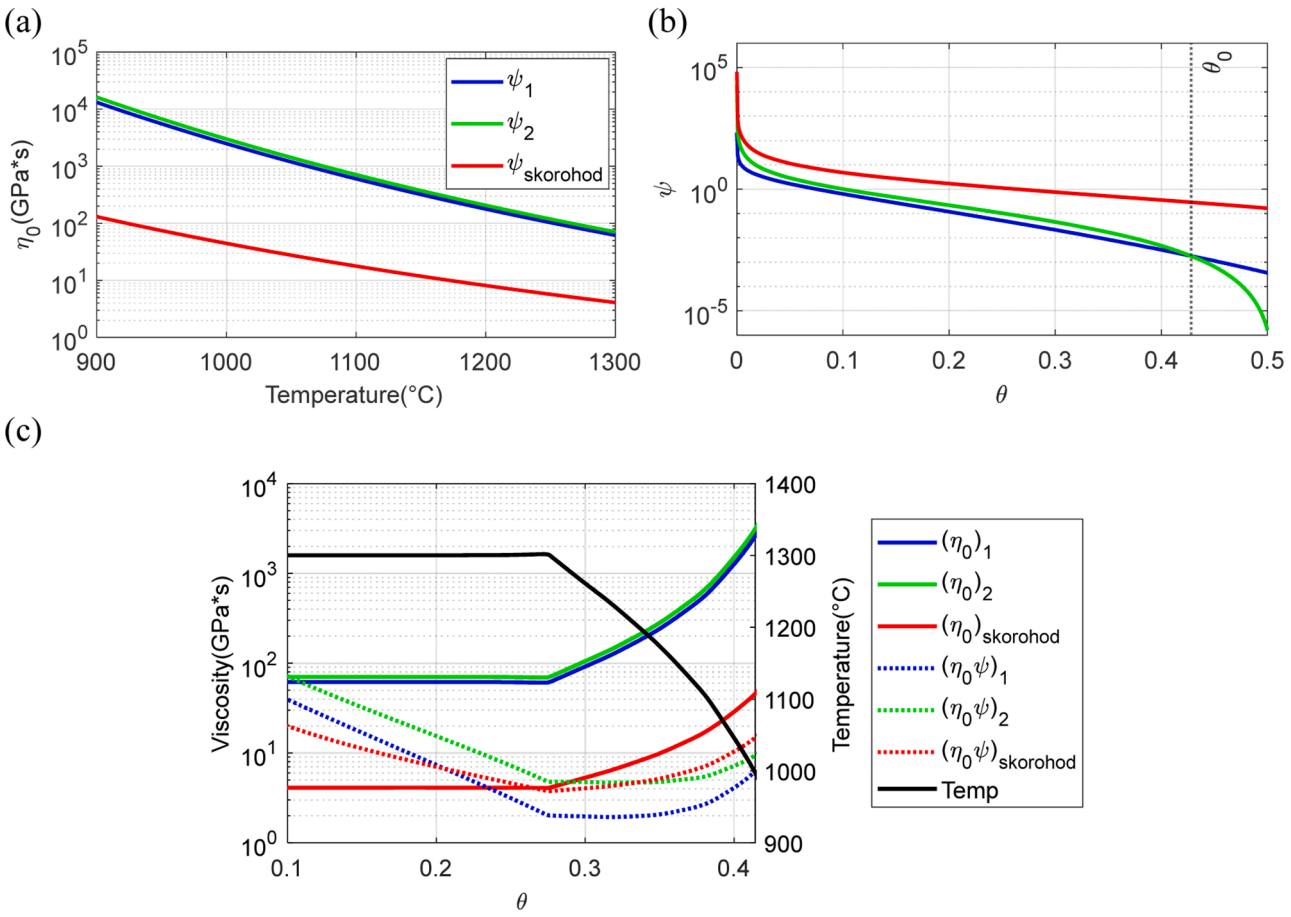

Fig. 7. Parameter curves for each model case studied: (a) shear viscosity η_0, (b) ψ normalized bulk modulus and (c) material shear viscosity η_0 and effecttive bulk viscosity $K = \eta_0\ \psi$ calculated using the experimental 1300 °C-600 min experimental data.

decreases as the porosity decreases. The smaller discrepancy with Skorohod module at low porosity can be related to a possible heterogeneous distribution of the pores in BJ samples [4,5].

As seen in Fig. 7(b), ψ_1 and ψ_2 are almost parallel for porosities higher than θ_0 (the identification region). Thus, both expressions are expected to have similar ability to describe the porosity dependence of the effective bulk viscosity. Fig. 7(c) shows that all K values are within the same order of magnitude. But the crucial difference lies in the evolution of the effective bulk viscosity with the porosity, evident during the isothermal step. Particularly, $(\eta_0 \cdot \psi)_{Skorohod}$ differs from the other cases because its value increases at a lower rate during the isothermal step. In this case, the porosity dependence of the effective bulk viscosity is fixed by the Skorohod normalized bulk modulus.

The fitting algorithm used allows for the utilization of experimental data from several individual sintering experiments simultaneously. As detailed in Appendix A, the utilization of such algorithms should be done carefully, in particular when the differential equation derived has a non-linear dependency of the porosity and temperature variables. . Also, the stability of the non-linear regression solution is dependent on the range of data collected from experiments, so a proper design of the sintering cycles and selection of the data must be done to avoid mistaken solutions. The parameters of ψ_1 and ψ_2 proposed in this work, represent the potential influence of the pore structure morphology and topology on the resistance to densification of the BJ part. Therefore, it can be expected that varying the powder size distribution (PSD), printer system (e.g. recoating or printing mechanism) or printing parameters (e.g. recoating speed or layer thickness) could influence the normalized bulk viscosity parameters obtained. Further experimental data from samples with different porous structures created by the different BJ manufacturing variables (e.g. PSD and printing parameters) is needed to study its effect on the parameters proposed here.

4.4. Modelling of densification during sintering of BJ samples

To evaluate the model performance for each case, the differential equation system formed by Eqs. (18) and (20) was solved by using Runge-Kutta numerical method [44]. The time-temperature data from each 600 min dwell time dilatometry test was used. The geometry-based green porosity and the smallest grain size measured were used as input parameters for Eqs. (18) and (20), respectively. Then, introducing the material shear viscosity parameters (A_0/α, Q) and the porosity function $f(\theta)$ with its corresponding fitted parameters, the porosity evolution model results for each case were calculated and reported in Fig. 8. In general, the three models describe the densification evolution of the BJ samples with different degrees of accuracy. As expected, both ψ_1 and ψ_2 cases showed notable accuracy in the prediction of the porosity evolution during sintering. This demonstrates the ability of the parameterized normalized bulk moduli to represent the experimental data from the sintering of BJ samples. Despite the absence of any fitting parameter of Skorohod expression, the results obtained by this model show a good general description of the porosity evolution during the sintering regime studied.

The residual values ($\theta_{Model} - \theta_{Exp.}$) and root-mean-square error (RMSE) were calculated for each pair of the experimental-model curve datasets (see Fig. 9) to qualitatively evaluate the accuracy of the model. RMSE values are stacked as a bar graph for each normalized bulk viscosity case. Staked values reveal a good performance for both ψ_1 and ψ_2, with slightly lower RMSE for the ψ_1 case, showing a slightly better

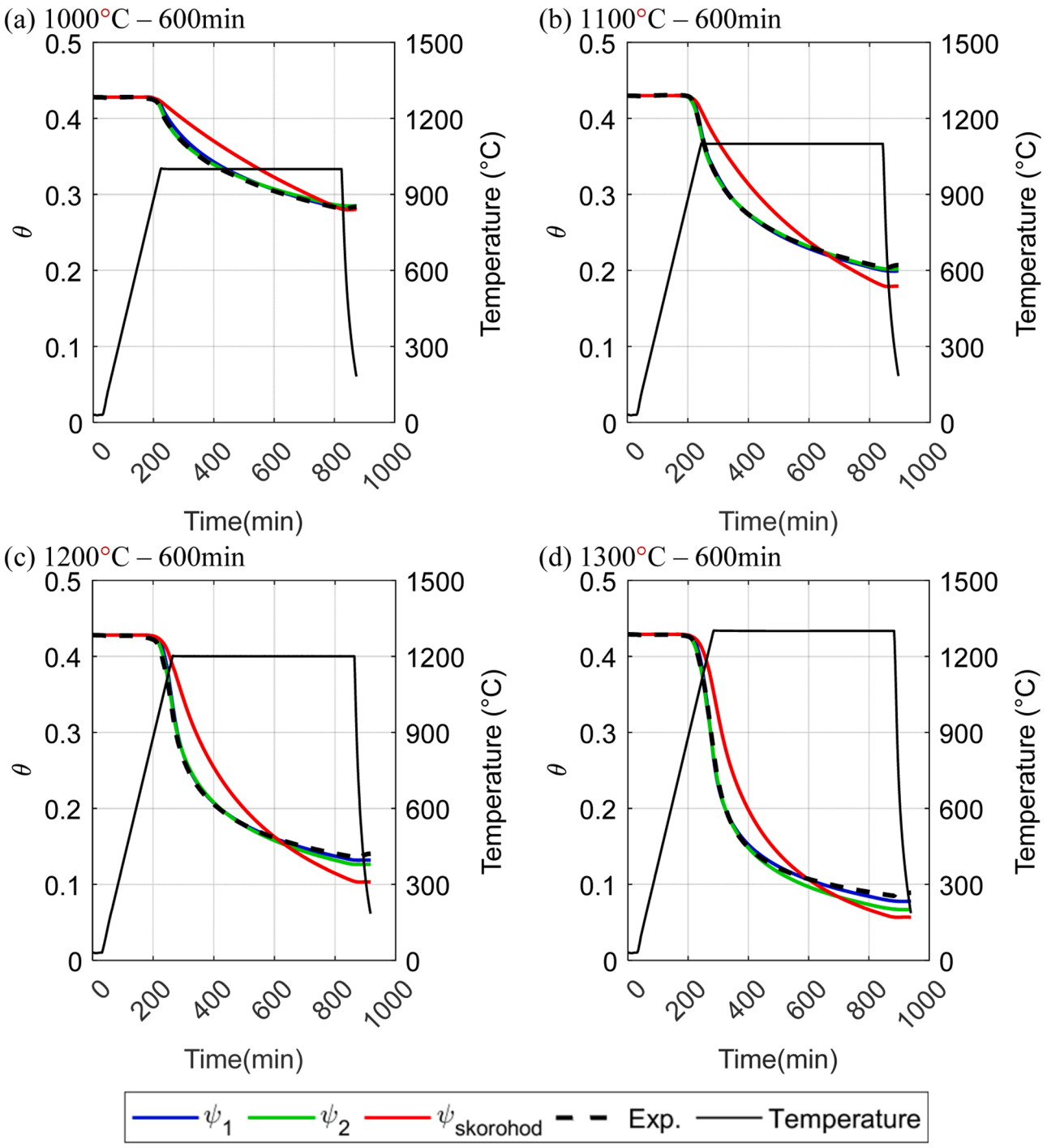

Fig. 8. Experimental and simulated densification for each different model case studied.

general behavior. Individually, ψ_1 RMSE values <0.45% are observed while ψ_2 showed a largest RMSE of 0.98% for the 1300 °C-600 min case. Looking in detail to the residuals in Fig. 9, the best porosity dependence behavior, within the lowest porosity region of the intermediate sintering step, is represented by the expression inspired by Hsueh model ψ_1.

The model inspired by the Abouaf studies is more accurate at high porosities close to the green value. But its accuracy decreases for smaller porosity levels <15% (see Fig. 8(d)). θ_c must be always lower than the green porosity, but it's still used as a fitting parameter. Thus, the physical meaning of θ_c is still ambiguous and need to be further studied. The model inspired by the Hsueh studies showed good accuracy for the prediction of sintering within all the ranges of porosity and temperature studied. This could be related to the ability of tailoring ψ_1 within the low and high porosity values via finding the best values of A and B. These parameters relate to stress concentrations located at the inter-particle contacts. Therefore, a correlation between the particle arrangement created by the BJ printing process and the values of these parameters is expected. During the initial stage of sintering, the interactions of inter-particle necks with each other are negligible, maintaining the topological structure specifics constant. But the powder packing determines the duration of this stage. Also, the intermediate step of sintering is dependent on the powder packing [2]. Accordingly, in the models proposed, the potential effect of the powder packing on the sintering is introduced in the normalized bulk modulus. Further research should be

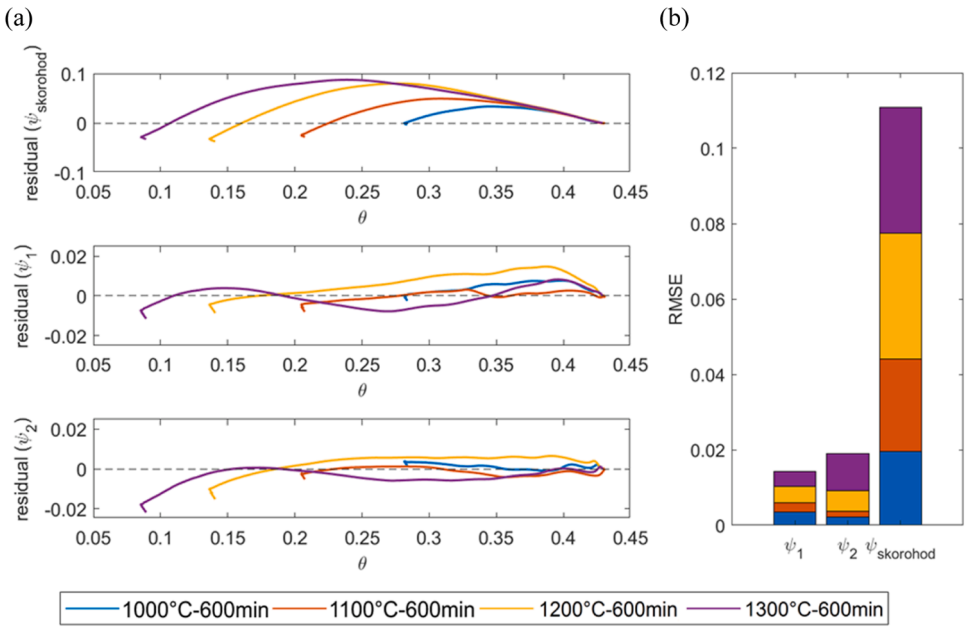

Fig. 9. Calculated residuals and root mean square error RMSE between the experimental and model densification curves for each model case studied.

carried out to clarify this complex relationship between the BJ printing process, porous green structure, and how it potentially affects the sintering model parameters.

5. Conclusions

The initial and intermediate step of sintering of BJ samples was analyzed using the continuum theory of sintering. Different normalized bulk viscosity moduli were considered, based on the Skorohod, Abouaf and Hsueh models. The experimental data required, and the methodology used for the model constants determination was developed based on the study of the complex non-lineal models obtained from different bulk viscosity moduli. Special attention was put in the stability of the non-linear regression solution from the fitting of experimental data. Consequently, dilatometry experiments at temperatures below the δ-ferrite transformation and long dwell times have been conducted. Interrupted sintering tests were performed, and the average grain size was characterized by a combination of a LOM image analysis and EBSD data. Significant grain growth (up to ~ 40 μm) was observed for the sintering at higher temperatures (1300 °C) and longer times (600 min), despite the relatively high porosity (~10%). Isotropic pressure-less sintering model parameters, including grain growth kinetics, were successfully determined. The model based on Skorohod moduli exhibited good global porosity prediction for the different temperatures studied, considering the absence of any fitting parameters. The models inspired by Abouaf and Hsueh studies included fitting parameters in the normalized bulk viscosity ψ, which improved the ability to tailor the model behavior with the experiments. These parameters relate to the particularities of the particles arrangement of green compacts manufactured by binder jetting. Despite the physical description of the critical porosity θ_C in Abouaf's model, its value is still ambiguous. By definition, this must be higher than the green porosity, so the bulk modulus function domain is defined at least from the green porosity (θ_0=0.428). But an explicit way to calculate this value is missing and its value θ_0=0.508 (obtained by fitting experimental data) is not explicitly related to the green porosity. In general, residuals and RMSE values showed that Hsueh modulus led to the best predictions with an RMSE <0.45% for all of the conditions studied. The modification proposed by Hsueh is related to the stress concentration at the inter-particle contacts. Thus, this effect is expected to be noticeable for the initial and intermediate sintering of BJ samples. Furthermore, the influence of the variation of BJ porous structure morphology (determined by powder size distribution or printing parameters) on the normalized bulk viscosity can be further studied using the methodology developed in the present study. Then, possible physical relation of the fitting parameters with the BJ porous morphology could be elucidated. In general, the results show that parametrized normalized bulk viscosity equations are more suitable to precisely reproduce the sintering behavior below the delta-ferrite transformation temperature and up until ~90% relative density. The method described in this study can be used to model the pressure-less isotropic sintering of low green density compacts, which experience solid-state sintering without phase transformations.

Declaration of Competing Interest

The authors declare that they have no known competing financial interests or personal relationships that could have appeared to influence the work reported in this paper.

Acknowledgments

This work was conducted in the framework of the center for Additive Manufacturing – Metal (CAM^2), supported by the Swedish Governmental Agency of Innovation Systems (Vinnova). The support of the US National Science Foundation (Collaborative Grants DMREF-2119832 and DMREF-2119833) is gratefully appreciated.

Supplementary materials

Supplementary data associated with this article can be found, in the online version, at 10.1016/j.actamat.2023.118822.

Appendix A: Numerical determination of sintering model parameters

The numerical determination of the model parameters is one of the essential steps in any phenomenological sintering model development process. Even if literature values can be used as material constants for sintering models, the results should be validated against the appropriate envelope of sintering experimental data. In some cases, the model used allows for the linearization of the derived equations to fit the model constants to experimental data ($T, \theta, \dot{\theta}, G$). However, in other cases, the derived equations have a non-linear dependency on some of the dependent variables (e.g. polynomial ratios or power functions). Therefore, in the presented study, a non-linear least squares numerical formulation was used to fit any of the presented models to the experimental data.

The other important aspect is related to the design of experiments to gather the appropriate experimental data set. No approach is perfect for all non-linear models, data sets, and starting points due to the nature of the approximation process. So, the numerical stability of the solution for a specific non-linear problem should be analyzed carefully. Ideally, the experimental data used for a problem should cover the widest envelope of values for the dependent variables studied. Consequently, dilatometry experiments were designed for long times (600 min) to cover a wide range of porosity values at different temperatures (1000 to 1300 °C). Also, potentially noisy data should be avoided during transition steps in our experimental procedures. So, the data collected during the isothermal sintering step was used, when the dilatometry system measurements become steady.

To validate the methodology presented in this study, two different cases were evaluated to demonstrate the importance of the concepts explained above. In both cases, the first model (ψ_1) was used, where the non-linear model equation was obtained from Eqn. (21) and (16). Then, three combinations for the model fitting constants starting values were evaluated (see Table A.1). In the first evaluation case, the experimental dataset was reduced to just one sintering experiment (1300 °C–600 min). The second evaluation case was done by using the complete dataset with sintering at different temperatures (identical to the data used in the core of the paper). Then, the non-linear least squares numerical method was applied in each case to find the necessary model parameters (A_0/α, Q, A and B). The parameter values for each evaluation case are detailed in Table A.1.

$$G\frac{d\theta}{dt} = -\frac{9}{2\frac{A_0}{\alpha}T\exp\left(\frac{Q}{RT}\right)}\cdot f(\theta) \tag{20}$$

The results obtained from the first evaluation case are presented in Fig. A.1. The 3D graph represents the different solution surfaces $G\frac{d\theta}{dt} = f(\theta, T)$ compared with all the experimental datasets. It can be observed that all the surfaces converged only through the used experimental dataset (1300 °C–600 min). However, these surfaces are different from each other and then lead to different model parameters (see Table A.1). This means that there is no unique solution when only one sintering experiment was used for the fitting process. Consequently, the calculation of the porosity evolution for each solution leads to inaccurate results when the sintering process simulated is different from the one used for fitting.

The results for the second evaluation case are presented in Fig. A.2. In this case, the visual distinction between the solution surfaces is not possible

Table A.1
Fitted model parameters for each evaluation case, where different experimental datasets were used. For each case three different sets of initial values were used for the non-linear least squares problem and the solution values for each are detailed.

		Single dataset 1300 °C – 600min				ALL datasets			
		A_0/α	Q	A	B	A_0/α	Q	A	B
Upper limit		1000	300	5	22	1000	300	5	22
Lower limit		0	0	0	1	0	0	0	1
Starting values	**1**	10	1	1	7	10	1	1	7
	2	100	2	1	12	100	2	1	12
	3	500	3	1	17	500	3	1	17
Solution	**1**	66.90	105.1	2.423	3.02	2.02	217.2	0.49	11.35
	2	4.11	142.0	2.411	3.06	2.02	217.2	0.49	11.35
	3	213.86	100.0	2.123	4.25	2.03	217.2	0.49	11.35

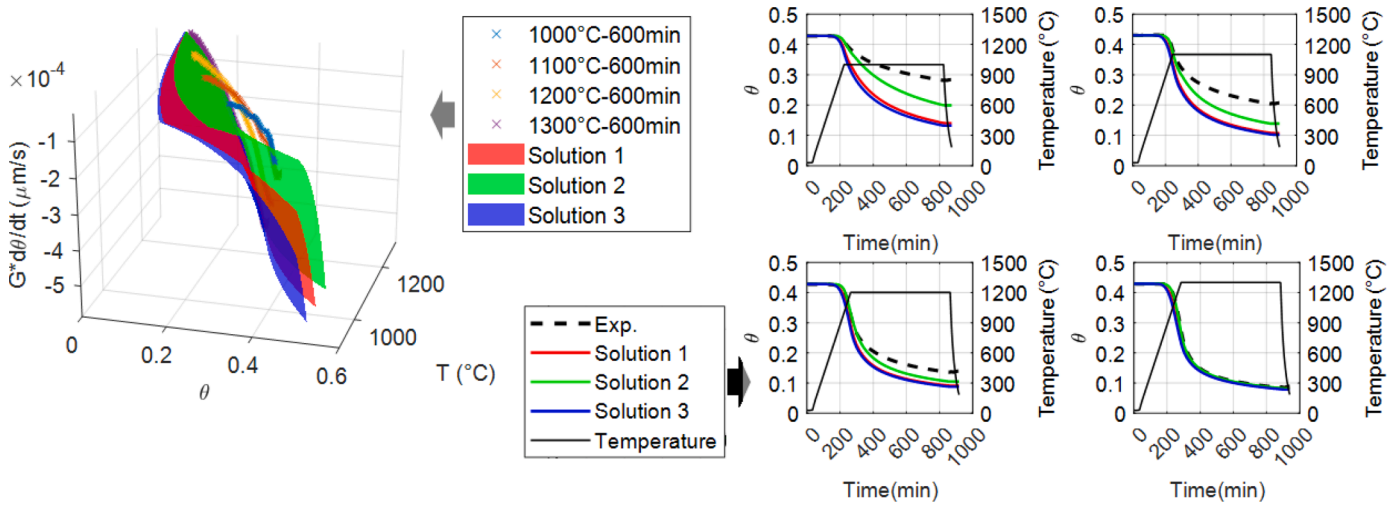

Fig. A1. Solution of the non-linear least squared problem for the evaluation case using just the data from sintering experiment 1300 °C – 600 min. Left graph shows the curves of the solution compared together with all the experimental datasets. Right graphs show porosity evolution using the parameters from each solution and the experimental data.

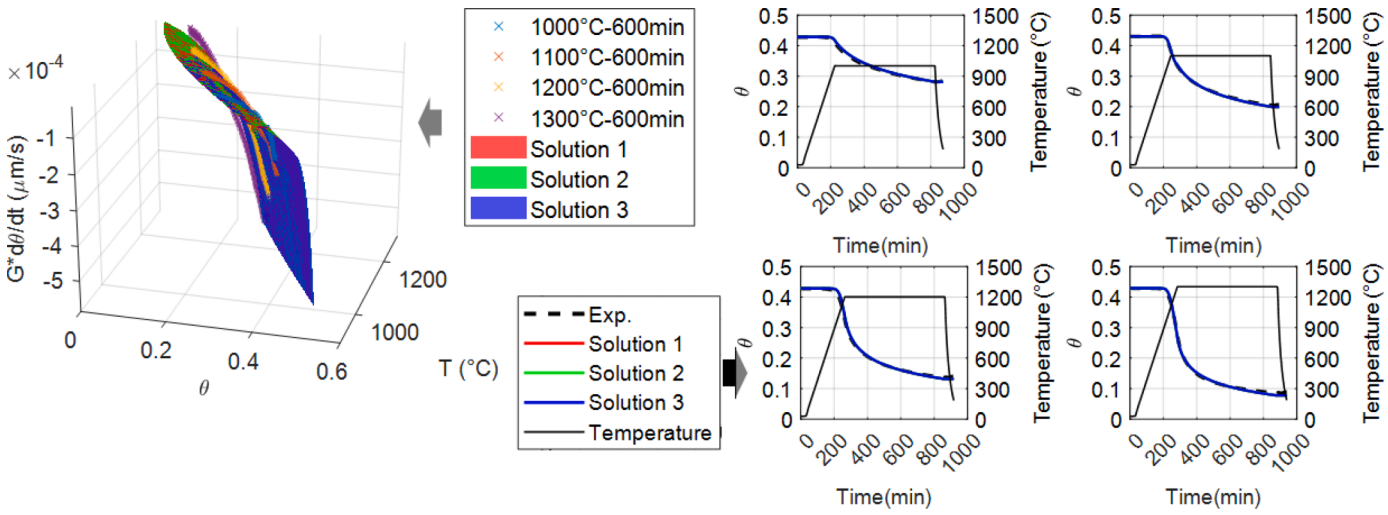

Fig. A2. Solution of the non-linear least squared problem for the evaluation case using all the datasets from experiments with a dwell time of 600 min (1000 °C, 1100 °C, 1200 °C and 1300 °C). Left graph shows the curves of the solution compared together with all the experimental datasets. Right graphs show porosity evolution using the parameters from each solution and the experimental data.

because all the initial values combinations converged to the same solution (see Table A.1). Also, it can be observed that the surface solutions reasonably converged through all the experimental dataset points. Therefore, in this case the use of the appropriate experimental dataset and a non-linear model lead to the convergence of the non-linear least squares problem to a unique solution, independently of the initial values used. Consequently, this leads to accurate model predictions of the density evolution when different sintering temperature and time routes are used.

In conclusion, the development of an appropriate methodology for the determination of the model parameters is a key part of the sintering model development. The algorithms and numerical methods need to be carefully used and their stability must be addressed. Also, the design of experiments should be appropriately developed according to the scope and limitations of the model developed. In this Appendix, the stability and suitability of the numerical methodology used in the present study is discussed.

References

[1] E.A. Olevsky, Theory of sintering: from discrete to continuum, Mater. Sci. Eng. R Rep. 23 (1998) 41–100, https://doi.org/10.1016/S0927-796X(98)00009-6.

[2] A.L. Maximenko, E.A. Olevsky, Effective diffusion coefficients in solid-state sintering, Acta Mater. 52 (2004) 2953–2963, https://doi.org/10.1016/j.actamat.2004.02.042.

[3] ISO/ASTM52900-21, Standard Terminology for Additive Manufacturing – General Principles – Terminology, ASTM International, West Conshohocken, PA, 2021.

[4] A. Cabo Rios, E. Hryha, E. Olevsky, P. Harlin, Sintering anisotropy of binder jetted 316L stainless steel: part II – microstructure evolution during sintering, Powder Metall. 65 (2022) 283–295, https://doi.org/10.1080/00325899.2021.2020486.

[5] A. Cabo Rios, E. Hryha, E. Olevsky, P. Harlin, Sintering anisotropy of binder jetted 316L stainless steel: part I – sintering anisotropy, Powder Metall 65 (2022) 273–282, https://doi.org/10.1080/00325899.2021.2020485.

[6] A. Mostafaei, A.M. Elliott, J.E. Barnes, F. Li, W. Tan, C.L. Cramer, P. Nandwana, M. Chmielus, Binder jet 3D printing—Process parameters, materials, properties, modeling, and challenges, Prog. Mater. Sci. 119 (2021), 100707, https://doi.org/10.1016/j.pmatsci.2020.100707.

[7] R.K. Bordia, S.J.L. Kang, E.A. Olevsky, Current understanding and future research directions at the onset of the next century of sintering science and technology, J. Am. Ceram. Soc. 100 (2017) 2314–2352, https://doi.org/10.1111/jace.14919.

[8] E.A. Olevsky, C. Garcia-Cardona, W.L. Bradbury, C.D. Haines, D.G. Martin, D. Kapoor, Fundamental aspects of spark plasma sintering: II. finite element analysis of scalability, J. Am. Ceram. Soc. 95 (2012) 2414–2422, https://doi.org/10.1111/j.1551-2916.2012.05096.x.

[9] E. Olevsky, T.T. Molla, H.L. Frandsen, R. Bjørk, V. Esposito, D.W. Ni, A. Ilyina, N. Pryds, Sintering of multilayered porous structures: part I-constitutive models, J. Am. Ceram. Soc. 96 (2013) 2657–2665, https://doi.org/10.1111/jace.12375.

[10] J.A. Alvarado-Contreras, E.A. Olevsky, R.M. German, Modeling of gravity-induced shape distortions during sintering of cylindrical specimens, Mech. Res. Commun. 50 (2013) 8–11, https://doi.org/10.1016/j.mechrescom.2013.02.007.

[11] J.A. Alvarado-Contreras, E.A. Olevsky, A.L. Maximenko, R.M. German, A continuum approach for modeling gravitational effects on grain settling and shape distortion during liquid phase sintering of tungsten heavy alloys, Acta Mater. 65 (2014) 176–184, https://doi.org/10.1016/j.actamat.2013.10.059.

[12] D. Giuntini, I.W. Chen, E. Olevsky, Sintering shape distortions controlled by interface roughness in powder composites, Scr. Mater. 124 (2016) 38–41, https://doi.org/10.1016/j.scriptamat.2016.06.024.

[13] C. Manière, T. Zahrah, E.A. Olevsky, Fluid dynamics thermo-mechanical simulation of sintering: uniformity of temperature and density distributions, Appl. Therm. Eng. 123 (2017) 603–613, https://doi.org/10.1016/j.applthermaleng.2017.05.116.

[14] C. Manière, S. Chan, E.A. Olevsky, Microwave sintering of complex shapes: from multiphysics simulation to improvements of process scalability, J. Am. Ceram. Soc. 102 (2018) 611–620, https://doi.org/10.1111/jace.15892.

[15] Y. Lee, P. Nandwana, S. Simunovic, Powder spreading, densification, and part deformation in binder jetting additive manufacturing, Prog. Addit. Manuf. (2021), https://doi.org/10.1007/s40964-021-00214-1.

[16] K. Zhang, W. Zhang, R. Brune, E. Herderick, X. Zhang, J. Cornell, J. Forsmark, Numerical simulation and experimental measurement of pressureless sintering of stainless steel part printed by binder jetting additive manufacturing, Addit. Manuf. 47 (2021), 102330, https://doi.org/10.1016/j.addma.2021.102330.

[17] S.J. Park, S.H. Chung, J.L. Johnson, R.M. German, Finite element simulation of liquid phase sintering with tungsten heavy alloys, Mater Trans. 47 (2006) 2745–2752, https://doi.org/10.2320/matertrans.47.2745.

[18] Z.Z. Du, A.C.F. Cocks, Constitutive models for the sintering of ceramic components-II. Sintering of inhomogeneous bodies, Acta Metall. Mater. 40 (1992) 1981–1994, https://doi.org/10.1016/0956-7151(92)90184-G.

[19] R.M. McMeeking, L.T. Kuhn, A diffusional creep law for powder compacts, Acta Metall. Mater. 40 (1992) 961–969, https://doi.org/10.1016/0956-7151(92)90073-N.

[20] C.H. Hsueh, A.G. Evans, R.M. Cannon, R.J. Brook, Viscoelastic stresses and sintering damage in heterogeneous powder compacts, Acta Metall. 34 (1986) 927–936, https://doi.org/10.1016/0001-6160(86)90066-0.

[21] K.R. Venkatachari, R. Raj, Shear deformation and densification of powder compacts, J. Am. Ceram. Soc. 69 (1986) 499–506, https://doi.org/10.1111/j.1151-2916.1986.tb07452.x.

[22] M.N. Rahaman, L.C. de Jonghe, G.W. Scherer, R.J. Brook, Creep and densification during sintering of glass powder compacts, J. Am. Ceram. Soc. 70 (1987) 766–774, https://doi.org/10.1111/j.1151-2916.1987.tb04877.x.

[23] V.V. Skorohod, Rheological basis of the theory of sintering, (1972).

[24] M. Abouaf, J.L. Chenot, G. Raisson, P. Bauduin, Finite element simulation of hot isostatic pressing of metal powders, Int. J. Numer. Methods Eng. 25 (1988) 191–212, https://doi.org/10.1002/nme.1620250116.

[25] E.A. Olevsky, V. Tikare, T. Garino, Multi-scale study of sintering: a review, J. Am. Ceram. Soc. 89 (2006) 1914–1922, https://doi.org/10.1111/j.1551-2916.2006.01054.x.

[26] J. Besson, M. Abouaf, Rheology of porous alumina and simulation of hot isostatic pressing, J. Am. Ceram. Soc. 75 (1992) 2165–2172, https://doi.org/10.1111/j.1151-2916.1992.tb04479.x.

[27] G. Kerbart, C. Harnois, S. Marinel, C. Manière, Modeling the sintering trajectories of MgAl2O4 Spinel, Scr. Mater. 203 (2021), 114048, https://doi.org/10.1016/j.scriptamat.2021.114048.

[28] C. Manière, C. Harnois, S. Marinel, Porous stage assessment of pressure assisted sintering modeling parameters: a ceramic identification method insensitive to final stage grain growth disturbance, Acta Mater. 211 (2021), 116899, https://doi.org/10.1016/j.actamat.2021.116899.
[29] J. Song, T. Barriere, B. Liu, J.C. Gelin, G. Michel, Experimental and numerical analysis on sintering behaviours of injection moulded components in 316L stainless steel powder, Powder Metall. 53 (2010) 295–304, https://doi.org/10.1179/003258908X334212.
[30] J. Song, J.C. Gelin, T. Barrière, B. Liu, Experiments and numerical modelling of solid state sintering for 316L stainless steel components, J. Mater. Process. Technol. 177 (2006) 352–355, https://doi.org/10.1016/j.jmatprotec.2006.04.111.
[31] M. Sahli, A. Lebied, J.C. Gelin, T. Barrière, B. Necib, Numerical simulation and experimental analysis of solid-state sintering response of 316L stainless steel micro-parts manufactured by metal injection molding, Int. J. Adv. Manuf. Technol. 79 (2015) 2079–2092, https://doi.org/10.1007/s00170-015-6983-8.
[32] C. van Nguyen, Y. Deng, A. Bezold, C. Broeckmann, A combined model to simulate the powder densification and shape changes during hot isostatic pressing, Comput. Methods Appl. Mech. Eng. 315 (2017) 302–315, https://doi.org/10.1016/J.CMA.2016.10.033.
[33] ASTM B962–17, Standard Test Methods For Density of Compacted or Sintered Powder Metallurgy (PM) Products Using Archimedes' Principle, ASTM International, West Conshohocken, PA, USA, 2013, https://doi.org/10.1520/B0962-17.2.
[34] P. Lehto, H. Remes, T. Saukkonen, H. Hänninen, J. Romanoff, Influence of grain size distribution on the Hall–Petch relationship of welded structural steel, Mater. Sci. Eng. A 592 (2014) 28–39, https://doi.org/10.1016/J.MSEA.2013.10.094.
[35] ASTM E112-10, Standard Test Methods For Determining Average Grain Size, ASTM International, West Conshohocken, PA, USA, 2010, https://doi.org/10.1520/E0112-13.1.4.
[36] M.W. Reiterer, K.G. Ewsuk, J.G. Argüello, An arrhenius-type viscosity function to model sintering using the Skorohod-Olevsky viscous sintering model within a finite-element code, J. Am. Ceram. Soc. 89 (2006) 1930–1935, https://doi.org/10.1111/j.1551-2916.2006.01041.x.
[37] C. Manière, G. Lee, J. McKittrick, S. Chan, E.A. Olevsky, Modeling zirconia sintering trajectory for obtaining translucent submicronic ceramics for dental implant applications, Acta Mater. 188 (2020) 101–107, https://doi.org/10.1016/j.actamat.2020.01.061.
[38] C. Manière, S. Chan, G. Lee, J. McKittrick, E.A. Olevsky, Sintering dilatometry based grain growth assessment, Results Phys. 10 (2018) 91–93, https://doi.org/10.1016/j.rinp.2018.05.014.
[39] I. Griva, S.G. Nash, A. Sofer, Nonlinear least squares data fitting, Linear Nonlinear Optim. 1 (2008) 764.
[40] R.M. German, Coarsening in sintering: grain shape distribution, grain size distribution, and grain growth kinetics in solid-pore systems, Crit. Rev. Solid State Mater. Sci. 35 (2010) 263–305, https://doi.org/10.1080/10408436.2010.525197.
[41] C. Manière, L. Durand, A. Weibel, C. Estournès, A predictive model to reflect the final stage of spark plasma sintering of submicronic α-alumina, Ceram. Int. 42 (2016) 9274–9277, https://doi.org/10.1016/j.ceramint.2016.02.048.
[42] G. Kerbart, C. Manière, C. Harnois, S. Marinel, Predicting final stage sintering grain growth affected by porosity, Appl. Mater. Today (2020) 20, https://doi.org/10.1016/j.apmt.2020.100759.
[43] Randall M. German, Novel sintering techniques, Sinter. Theory Pract. (1996) 373–420.
[44] J.R. Dormand, P.J. Prince, A family of embedded Runge-Kutta formulae, J. Comput. Appl. Math. 6 (1980) 19–26, https://doi.org/10.1016/0771-050X(80)90013-3.